Multi-Mission Sea Surface Salinity Optimum interpolation (OISSS) Analysis Version 3.0

Oleg Melnichenko[1], Peter Hacker[2], Thomas Meissner[3], Frank Wentz[3], Julian Schanze[1], and Jesse Anderson[1]

[1] Earth and Space Research, Seattle, Washington
[2] Hawaii Institute of Geophysics and Planetology, School of Ocean and Earth Science and Technology, University of Hawaii, Honolulu, Hawaii
[3] Remote Sensing Systems, Santa Rosa, California

ESR Technical Report ESR-TR-2026-001

May 1, 2026

Table of Content

1. Overview of v3.0 release…….. 2
2. Summary of updates from v2.0 to v3.0…… 3
3. Algorithm overview……... 3
4. Satellite SSS data and data processing……..... 4
    4.1. Satellite SSS data…….…….. 4
    4.2. Data quality control……... 7
    4.3. Bias correction…….. 9
    4.4. Noise reduction……. 12
5. Optimum Interpolation analysis…… 14
    5.1. General description…… 14
    5.2. Specifics……. 14
        5.2.1. First guess…….. 14
        5.2.2. Signal statistics…….. 15
        5.2.3. Error statistics…… 16
    5.3. Implementation…….. 18
    5.4. Uncertainty estimate ……. 19
        5.4.1. Empirical uncertainty ……... 19
        5.4.2. Formal uncertainty …… 19
6. Global OISSS fields…….. 19
    6.1. Spatial coverage and resolution…….…… 20
    6.2. Validation……..... 21
7. Acknowledgements…… 25
8. References…….. 25
9. Data format specification…… 28

1. Overview of v3.0 release

This technical note describes version 3.0 (v3.0) of the multi-mission sea surface salinity optimum interpolation (OISSS) analysis.

The OISSS dataset integrates observations from NASA's Aquarius/SAC-D, Soil Moisture Active-Passive (SMAP) and the European Space Agency's Soil Moisture and Ocean Salinity (SMOS) satellite missions to produce a continuous and consistent multi-satellite sea surface salinity (SSS) record.

The OISSS dataset is provided on a regular 0.25° x 0.25° latitude-longitude spatial grid and covers the period from 2011 to the present. The analysis is based on Optimum Interpolation (OI), utilizes Level 2 orbital data, and applies satellite-specific bias-correction algorithms to adjust satellite retrievals for biases with respect to in-situ observations.

The OISSS v3.0 dataset also provides computations of the monthly mean, monthly climatological mean and monthly SSS anomaly fields.

The consistency and accuracy of the OISSS v3.0 dataset have been evaluated against in situ salinity observations from Argo floats and moored buoys. The global mean root-mean-square difference (RMSD) between OISSS v3.0 and concurrent in situ measurements is approximately 0.22 psu. The mean global bias is zero.

The product follows CF/ACDD metadata conventions and includes an estimated SSS uncertainty field.

Release Date: 05/01/2026

Data Access:

- ESR web site: https://www.esr.org/data-products/oisss/
- PO.DAAC: TBD

2. Summary of updates from V2.0 to V3.0

- ✓ SMOS observations (Level 2 OS version 700) are included over the entire period of the dataset (i.e. not only to fill gaps in SMAP observations as in OISSS v2.0).
- ✓ The data are processed at full spatial resolution.
- ✓ Improved bias-correction algorithms are implemented to account for systematic instrument biases in satellite SSS retrievals. Measurements from the SMOS satellite are calibrated relative to SMAP SSS, including corrections for spurious seasonal variability.
- ✓ Additional noise-reduction algorithms are implemented to reduce high-frequency instrument noise.
- ✓ Spatial OI is applied to 4-day Level 2 SSS data (instead of 8-day as in OISSS v2.0) with a 4-day time step. This improves temporal resolution of the dataset.
- ✓ Temporal OI is applied to 4-day SSS maps to produce daily time series.
- ✓ Improved estimates of the signal and error statistics are incorporated into the OI algorithm. The correlation scales are derived from a spatiotemporal analysis of the satellite SSS data (Yi et al., 2022, Remote Sensing, 14(21), 5435).

The description of the algorithm below follows the original description of the algorithm as in versions v1.0 and v2.0, but reflects the updates and changes summarized above.

2. Algorithm overview

A schematic diagram of the OISSS v3.0 analysis is shown in Figure 1.

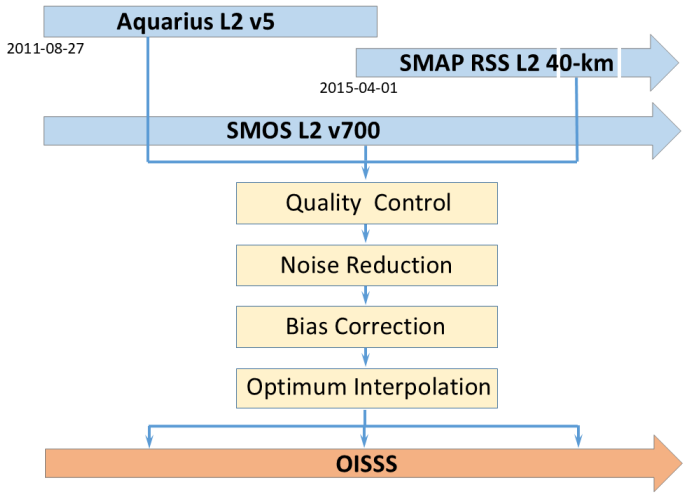

Figure 1. Schematic diagram of the OISSS v3.0.

The input data consist of Level 2 SSS retrievals from the Aquarius, SMAP, and SMOS satellites, described in Section 4.1. The first step in the processing algorithm involves quality control of the Level 2 data. Quality control flags and related auxiliary information (e.g., SST and surface winds) provided in the data files are used for this purpose. The quality control procedures are described in Section 4.2.

The next step in data processing consists of a large-scale adjustment of the satellite SSS data relative to in-situ data. **The algorithm corrects the satellite data only for persistent (time-mean) biases, which are determined independently for Aquarius and SMAP observations.** The bias-correction algorithms are described in Section 4.3. **SMOS SSS data are subsequently adjusted relative to the bias-corrected SMAP SSS** (Section 4.3.3).

In the final step, gridded SSS fields are produced using the Optimum Interpolation (OI) algorithm described in detail in Section 5. The output (Section 6) consists of time series of SSS fields generated using a unified processing algorithm.

4. Satellite SSS data and data processing

4.1 Satellite SSS data

4.1.1. Aquarius SSS data

The Aquarius/SAC-D satellite mission provided observations of SSS from August 2011 to June 2015. The satellite was positioned on a polar sun-synchronous orbit crossing the equator at 6 pm (ascending) and 6 am (descending) local time with a repeat cycle of 7 days. The Aquarius instrument consisted of three microwave radiometers that generated three beams at different angles relative to the sea surface. The beams had elliptical footprints on the sea surface (76 x 94 km, 84 x 120 km, and 96 x 156 km) aligned across a ~390-km-wide swath (Figure 2a). The emission from the sea surface, measured by the radiometers as an equivalent brightness temperature (Tb), was converted to SSS, subject to corrections for various geophysical effects. A detailed description of the Aquarius/SAC-D satellite mission and the Aquarius instrument can be found in Le Vine et al. (2007).

The Aquarius observations of SSS have been obtained from Level 2 version 5.0 (end-of-mission) Aquarius data produced by the NASA Goddard Space Flight Center's Aquarius Data Processing System (ADPS). The Level 2 data files, distributed by the Physical Oceanography Distributed Active Archive Center (PO.DAAC) of the Jet Propulsion Laboratory (JPL), contain retrieved SSS, navigation data, ancillary fields, quality flags, and other related information such as surface winds. The data are structured as a sequence of files, each corresponding to one orbit of Aquarius. An orbit is defined as starting when the satellite passes the South Pole. Individual observations along each orbit consist of a sequence of data points sampled at a 1.44-second (~10 km) interval. Each individual observation represents the average salinity in the upper 1-2 cm layer and over a ~100 km footprint (Le Vine et al., 2007; Lagerloef et al., 2008). A detailed description of Aquarius

data can be found in the Aquarius User Guide (Aquarius Dataset Version 5.0). The retrieval algorithm is described in Meissner et al. (2017, 2018).

An example of Aquarius Level 2 SSS data is presented in Figure 2. As illustrated in Figure 2, at least two types of errors are present in the SSS retrievals. One major source of error is associated with the accuracy of individual measurements along the satellite tracks. The instrument noise is essentially "white" in nature and can be reduced by filtering the data along the satellite tracks, as shown in Figure 2c (heavy lines). Another concern is the discrepancy between the three beams, which can reach 0.5–0.8 psu and appears to be correlated over large distances along the satellite tracks. These inter-beam biases are likely manifestations of residual errors in the geophysical corrections.

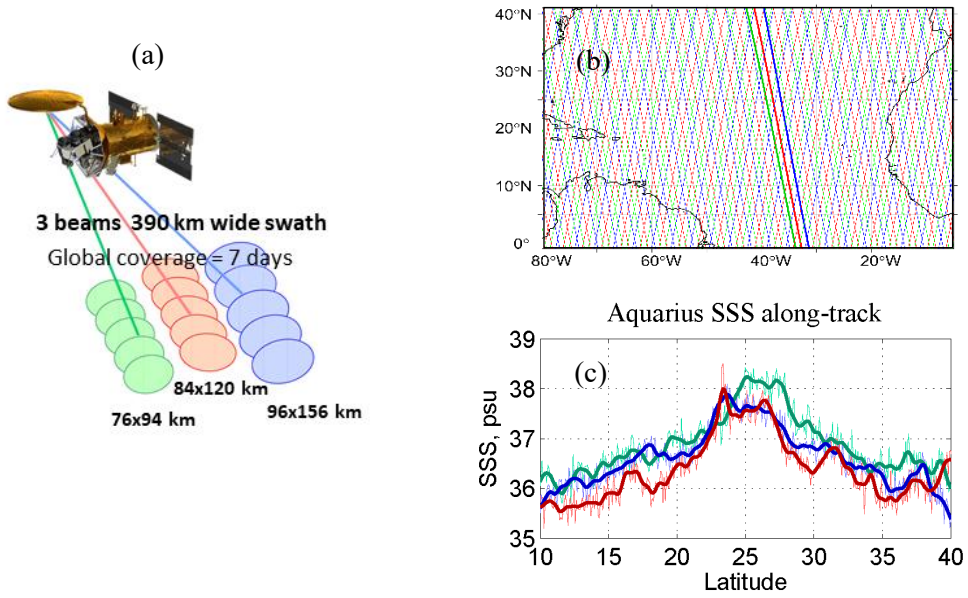

Figure 2. (a) Aquarius measurement geometry. (b) Example pattern of Aquarius ground tracks over the North Atlantic over a 7-day period. Colors indicate the three Aquarius beams. Ascending passes are from southeast to northwest. (c) Example of Level 2 SSS (three beams; 390-km-wide swath) passing through the subtropical North Atlantic on September 14, 2012 (thick lines in (b)). Thin curves – raw data; thick curves – smoothed with a running Hanning filter of half-width of ~60 km (approximately half-width of the Aquarius footprint). Colors indicate the three Aquarius beams.

4.1.2. SMAP SSS data

NASA's SMAP satellite, launched on January 31, 2015, started collecting SSS observations in April 2015, overlapping with Aquarius observations for about three-month period (April-June 2015). The satellite is positioned on a polar sun-synchronous orbit crossing the equator at 6 pm (ascending) and 6 am (descending) local time with a repeat cycle of 8 days. Similar to Aquarius, the measurement principle of SMAP is based on the response of the L-band sea surface brightness temperature (Tb) to SSS. The measuring

instrument is a large rotating antenna which provides Tb observations within approximately 1000-km wide swath with nominal resolution of about 40-km and a near global coverage in 3-4 days (Figure 3a).

SMAP observations of SSS have been obtained from Level 2 version 6.0 (version 6.3 from August 2023) SMAP SSS data produced by the Remote Sensing Systems (RSS; www.remss.com). SSS is retrieved on a 0.25° Earth grid using the 40-km spatial resolution Backus Gilbert optimum interpolation from the original Level 1 footprint measurements. The Level 2 data files contain retrieved SSS (variable 'sss_smap_40km'), navigation data, ancillary fields, quality flags, and other related information such as surface winds, sea surface temperature, etc. Each file corresponds to one orbit of SMAP. A detailed description of SMAP data and the retrieval algorithm can be found in Meissner et al. (2024). An example of SMAP Level 2 SSS data is shown in Figure 3b.

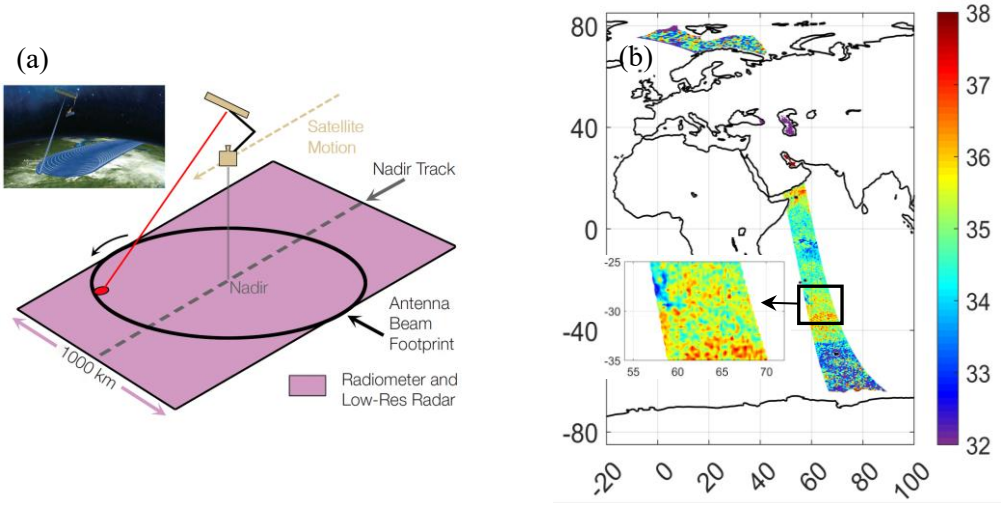

Figure 3. (a) SMAP measurement geometry. Credit: NASA. (b) Example of SMAP Level 2 SSS for the orbit passing through the Indian Ocean on April 1, 2015.

3.1.3. SMOS SSS data

In the OISSS v3.0, SMOS SSS data are included over the entire period of the dataset from September 2011 to the present.

The SMOS satellite, launched on November 2, 2009, operates on a sun-synchronous polar orbit crossing the equator at 6 am (ascending) and 6 pm (descending) local time. Its measuring instrument, MIRAS (Microwave Imaging Radiometer using Aperture Synthesis), is a two-dimensional L-band interferometric radiometer composed of an array of 69 receivers arranged in a Y-shaped configuration. The instrument provides measurements of Tb in an approximately 1000-km wide swath with spatial resolution of ~45 km and revisit time of 3-5 days.

SMOS observations of SSS have been obtained from the SMOS Level 2 SSS data products generated by version 700 of the Level 2OS Operational Processor (L2OS). SSS is retrieved

on a 25-km Equal-Area Scalable Earth (EASE) grid from Tb recorded by the MIRAS radiometer. The Level 2 data are structured as a sequence of files, each file containing half-orbit data (from pole to pole). The files contain retrieved SSS, navigation data, ancillary fields (surface winds, sea surface temperature, etc.), quality flags, and other related information. A detailed description of SMOS data and the retrieval algorithm can be found in SMOS L2 OS ATBD, https://earth.esa.int/eogateway/documents/20142/37627/SMOS-L2OS-ATBD.pdf. The data are available from the ESA SMOS online dissemination service at https://smos-diss.eo.esa.int/oads/access/.

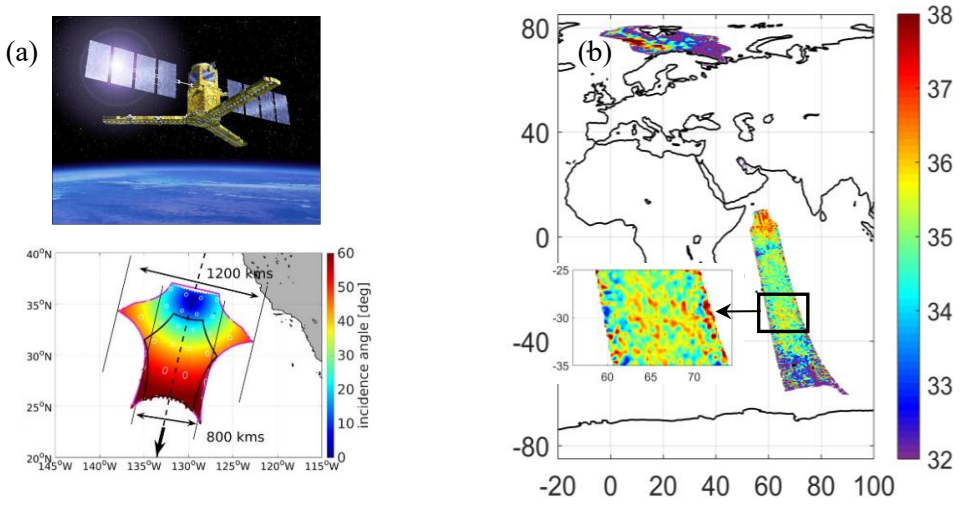

Figure 4. (a) SMOS measurement geometry. Bottom panel shows the shape of a Tb image as reconstructed from SMOS observations. Colors show incidence angle. Credit: ESA and Reul et al. (2020). (b) Example plot of SMOS Level 2 SSS for the orbit passing through the Indian Ocean on August 26, 2011.

An example of SMOS Level 2 SSS data is presented in Figure 4. Individual measurements along the orbit are very noisy. Retrievals near the edge of the swath typically have larger uncertainties due to a smaller number of observations and contaminations from various sources (Reul et al., 2017). SMOS SSS observations are also affected by significant large-scale biases arising from land or sea-ice emission contamination, which can extend as far as 1000 km from the coastline or sea-ice edge. Other sources of error include radio-frequency interference (RFI), uncertainties in the retrieval algorithm, and additional instrumental or environmental effects (Boutin et al., 2018).

4.2. Data quality control

Level 2 data from each of the three satellites are first processed to identify and address quality control (QC) issues. The specific QC procedures are different for each sensor and are described below.

4.2.1. Aquarius SSS data

Observations are discarded if the bits for any quality checks are set: 7 (direct solar flux contamination), 8 (reflected solar flux contamination), 9 (sun glint), 12 (non-nominal navigation), 13 (radiometer telemetry), 14 (roughness correction failure), 16 (pointing anomaly), 17 (brightness temperature consistency), 19 (radio-frequency interference (RFI)), and 21 (reflected radiation from Moon or Galaxy). In the case of flags 19 and 21, the data are excluded from the analysis if the conditions indicated by the flags are either moderate or severe. For other flags, the data are excluded if the conditions indicated by the flags are severe. Also excluded from the analysis are data points that are contaminated by land (land fraction > 0.01 (for internal seas this threshold is relaxed to 0.05)), sea ice (sea ice fraction > 0.0025), sampled during high wind (wind speed > 18 m/s) and/or in cold water (SST < 0ºC). A detailed description of the Aquarius quality flags including recommended thresholds can be found in the Aquarius User Guide (Aquarius Dataset Version 5.0).

4.2.2. SMAP SSS data

Observations are discarded if the bits for any of the following quality checks are set: the sun glint (bit 5 in Q/C flag, Table 5 in Meissner et al., 2024), moon glint (bit 6), reflected galactic radiation (bit 7), Tb consistency (bit 10), and RFI (bit 17; but only in version 6.3), Also excluded from the analysis are data points that are contaminated by land (gain weighted land fraction > 0.008 or land fraction in 3-dB footprint >0.0005 (for internal seas these thresholds are 0.04 and 0.005, respectively)), sea ice (sea ice fraction > 0.0025), sampled during high wind (wind speed > 18 m/s) and/or in cold water (SST < 0ºC). A detailed description of the SMAP quality flags can be found in Meissner et al. (2024).

4.2.2. SMOS SSS data

Observations are discarded if the following Quality Flags are set (Table 4-20 in SMOS Level-2 and Auxiliary Data Products Specifications document): outside range (bit 2), sun glint (bit 7), moon glint (bit 8), high galactic noise (bit 9), maximum number of iterations (bit 11), too few valid measurements (bit 12), low number of measurements (bit 13), many outliers (bit 14), high Marquardi increment (bit 15), and missing ECMWF data (bit 18).

Observations are discarded if the following Science Flags are set (Table 4-21 SMOS Level-2 and Auxiliary Data Products Specifications document): too close to land (bit 1), sea ice concentration above threshold (bit 5), suspect ice in grid point (bit 6), and high rain rate (bit 7). Also excluded from the analysis are data points that are near the edge of the swath (X_swath > 350 km), near a coastline (distance to the nearest coast < 60 km), measured during high wind (wind speed > 18 m/s) and/or in cold water (SST < 0ºC). In addition, observations are discarded if the overall data quality parameter Dg_af_fov is <130. A detailed description of SMOS quality flags can be found in the SMOS Level-2 Products Specifications document (https://earth.esa.int/eogateway/documents/20142/0/SMOS-L2-Aux-Data-Product-Specification.pdf).

4.3. Bias correction

The next step in data processing consists of a large-scale adjustment of the satellite data relative to in-situ data. Only static (time-mean) biases are taken into account.

Generally, the bias-adjusted satellite observations S_{adj} are determined from the retrieved values S_{obs} as

$$S_{adj} = S_{obs} - \Delta S\,, \qquad (1)$$

where the bias ΔS is determined by interpolating the bias fields into the locations of the satellite measurements. Specific procedures, however, are slightly different for Aquarius, SMAP and SMOS data.

4.3.1. Aquarius SSS data

Analysis of time series of Aquarius SSS data indicates that satellite retrievals exhibit large-scale biases relative to in situ observations (Kao et al., 2018).

In the OISSS analysis, large-scale biases in satellite SSS are corrected using in situ salinity observations as a reference. To account for the measurement geometry of the Aquarius satellite, the bias fields are constructed on a repeat-track basis. Specifically, satellite observations along each repeat track are averaged over a three-year period from September 2011 through August 2014 and compared with in-situ salinity averaged over the same period. The in-situ salinity data, treated here as the the large-scale "ground truth", is defined as the mean of four Argo-based products. The v3.0 release incorporates the following four products:

- JAMSTEC MOAA GVP global gridded salinity product produced by optimal interpolation of all available observations including ARGO (Hasoda et al., 2008; https://www.jamstec.go.jp/argo_research/dataset/moaagpv/moaa_en.html);
- Scripps Institution of Oceanography Argo-derived salinity product (http://sio-argo.ucsd.edu/RG_Climatology.html; Roemmich, D. and J. Gilson, 2009);
- Met Office Hadley Center objective analysis from the profile data, version EN.4.2.2 (http://hadobs.metoffice.com/en4/index.html; Good et al., 2013); and
- ISAS-20 salinity gridded fields (https://www.argo-france.fr/Argo-Data-Products/Argo-France-products/ISAS-products; Kolodziejczyk et al., 2021).

The mean of the four products is assumed to provide a more accurate representation of the "ground truth," provided that the mapping errors of the individual products are not correlated. Prior to the computation of the bias fields, both the along-track SSS and the "ground truth" fields were smoothed using a low-pass Hanning filter with a 4° half-width. The "ground truth" fields were subsequently interpolated onto the satellite ground-track locations, resulting in two bias fields corresponding to the ascending and descending tracks. The bias fields are shown in Figure 5.

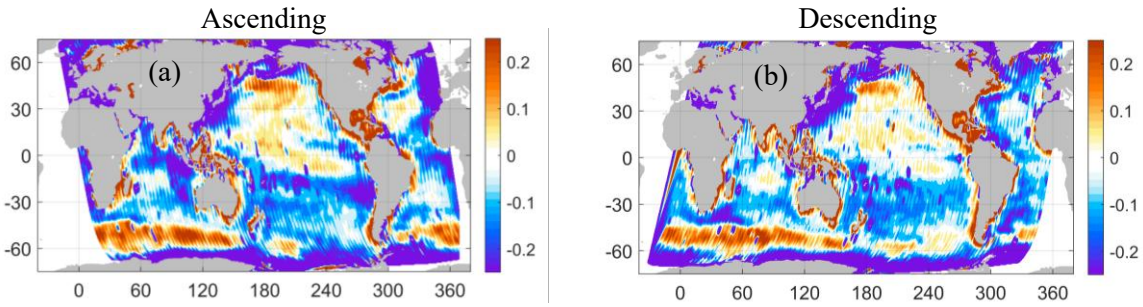

Figure 5. Mean spatial bias correction fields (psu) for Aquarius ascending (a) and descending (b) SSS data. Note that the bias fields are constructed on a specific (irregular) grid, which corresponds to the ground track segments.

Correcting for the large-scale satellite biases on a repeat track basis separately for each of the three Aquarius beams helps eliminate residual inter-beam biases.

4.3.2. SMAP SSS data

Persistent large-scale biases have been present in all versions of SMAP SSS data and are characterized by biases that appear in the long-term mean. To construct the bias field, satellite observations at each grid point were averaged over a four-year period from June 2015 through May 2019 and compared with the "ground truth" averaged over the same period. Different from v2.0, the "ground truth" in v3.0 was assessed as the average of the following four Argo-based products:

- JAMSTEC MOAA GVP global gridded salinity product produced by optimal interpolation of all available observations including ARGO (Hasoda et al., 2008; https://www.jamstec.go.jp/argo_research/dataset/moaagpv/moaa_en.html);
- Scripps Institution of Oceanography Argo-derived salinity product (http://sio-argo.ucsd.edu/RG_Climatology.html; Roemmich, D. and J. Gilson, 2009);
- Met Office Hadley Center objective analysis from the profile data, version EN.4.2.2 (http://hadobs.metoffice.com/en4/index.html; Good et al., 2013); and
- ISAS-20 salinity gridded fields (https://www.argo-france.fr/Argo-Data-Products/Argo-France-products/ISAS-products; Kolodziejczyk et al., 2021).

The SMAP bias field is shown in Figure 6. As there are almost no ascending-descending differences, the bias field is the same for ascending and descending data.

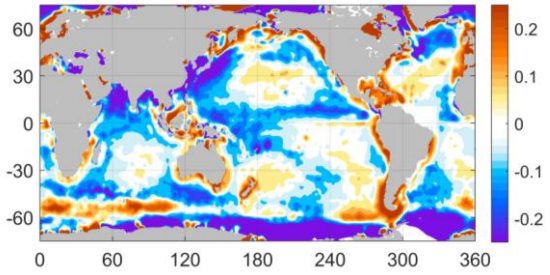

Figure 6. Mean spatial bias correction field (psu) for SMAP SSS data.

4.3.3. SMOS SSS data

SMOS SSS observations are adjusted for biases with respect to SMAP SSS.

The OISSS v3.0 algorithm uses the following procedure. At each grid point, the SSS time series from SMOS (ascending and descending averaged together in 4-day blocks) is compared with the bias-adjusted SSS time series from SMAP and the mean difference between the two is regarded as the time-mean bias for SMOS. An example for a single grid point is presented in Figure 7a. The bias is computed over a 7-year period from September 1, 2015, to August 31, 2022. The mean bias field for SMOS is shown in Figure 7b.

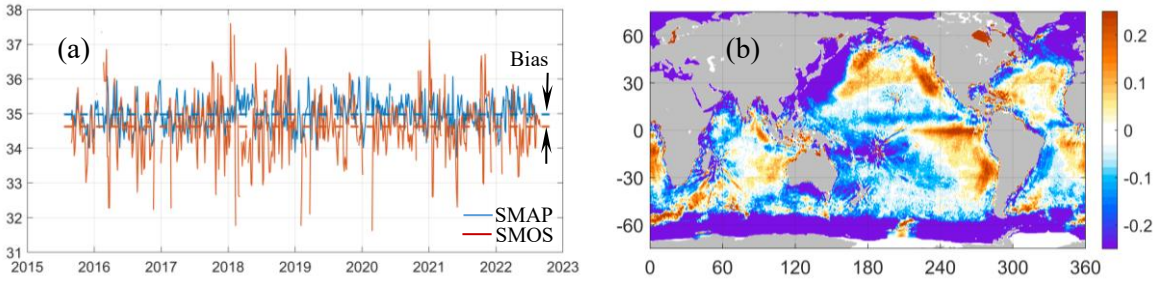

Figure 7. (a) Time series of SMAP (blue) and SMOS (red) SSS at a grid point 54°N, 335°E. The mean bias in SMOS observations is determined as the mean difference between the time series. (b) Mean spatial bias correction field (psu) for SMOS SSS data.

In addition, SMOS SSS observations are corrected for seasonal biases. These biases are estimated relative to SMAP SSS. At each grid point, the seasonal bias is computed as the sum of the annual and semiannual harmonics obtained through a least-squares fit to the time series of differences between SMOS and SMAP SSS:

$$\Delta S(t) = \Delta S_0 + A_{12}\cos(\omega_{12}t + \varphi_{12}) + A_6\cos(\omega_6 t + \varphi_6), \qquad (2)$$

where ΔS_0 is the time-mean bias (determined earlier, Fig. 7), ω_{12} and ω_6 are the annual and semiannual frequencies ($\omega_{12} = 2\pi/365\ days$, $\omega_6 = 2\pi/182.5\ days$), and A_{12}, A_6, φ_{12} and φ_6 are the associated amplitudes and phases.

The amplitudes and phases of the annual and semiannual harmonics of the seasonal biases in Eq. (2) are estimated from time series spanning the seven-year period from September 1, 2015, to August 31, 2022. An example for a single grid point is presented in Figure 8a. The spatial distribution of the amplitude of the seasonal bias in SMOS SSS is shown in Figure 8b.

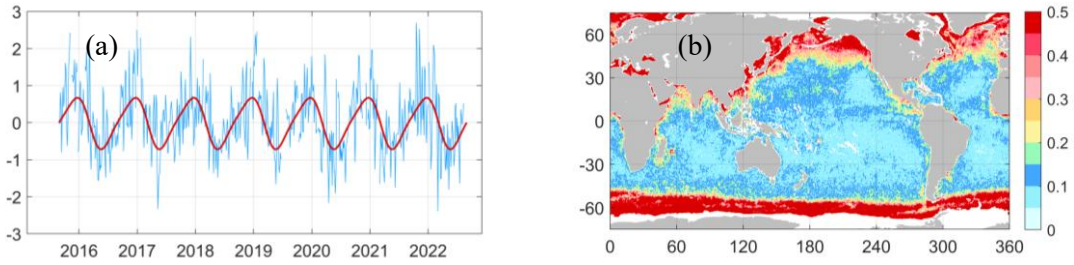

Figure 8. (a) Time series of the differences between SMOS and SMAP SSS (blue) at a grid point 52°N, 220°E and their approximation by the annual and semiannual harmonics (red). **(b)** amplitude of the seasonal bias in SMOS SSS.

The parametric representation in Eq. (2) enables the extension of the bias correction both backward and forward in time.

4.4. Noise reduction

The final step in data preparation consists of additional filtering to remove outliers and reduce noise.

4.4.1. Aquarius SSS data

Aquarius SSS data are filtered along-track following the methodology described in Melnichenko et al. (2014). The filtering procedure consists of the sequential application of a five-point median filter and a six-point Hanning filter. This approach has been shown to effectively reduce high-frequency instrumental noise while preserving the underlying oceanic signal from over-smoothing. An example is presented in Figure 1b.

4.4.2. SMAP SSS data

SMAP SSS data are filtered in the time domain. At each grid point, the SSS time series (derived from Level 2 SSS aggregated into 4-day intervals) is processed using a four-point (8-day half-width) Hanning filter. This filtering procedure reduces high-frequency instrumental noise and mitigates the effects of sub-grid-scale variability that are not resolved by the 8-day repeat observation cycle. An example is presented in Figure 9.

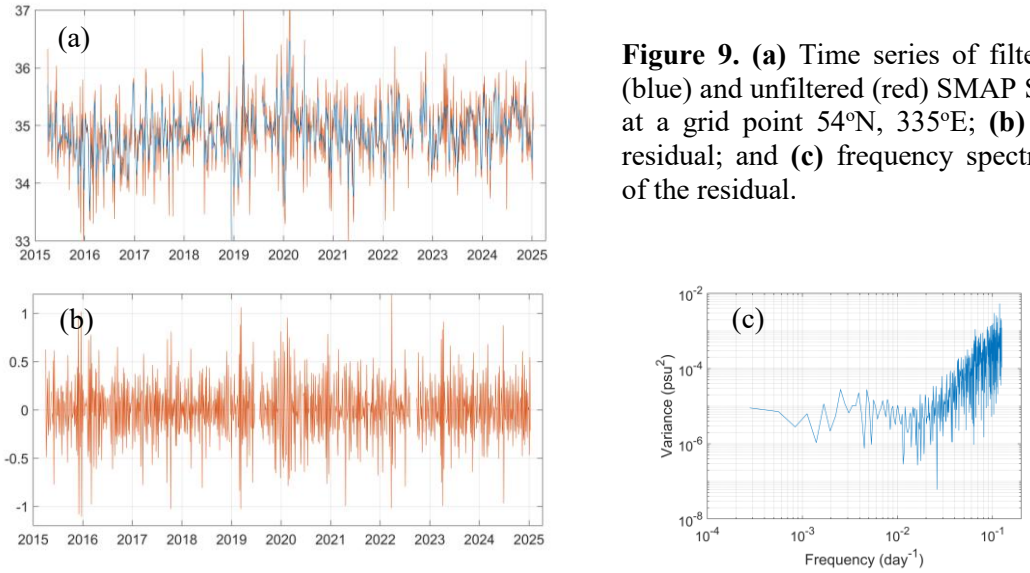

Figure 9. (a) Time series of filtered (blue) and unfiltered (red) SMAP SSS at a grid point 54°N, 335°E; **(b)** the residual; and **(c)** frequency spectrum of the residual.

Prior to OI, an additional standard statistical quality-control test based on the standard deviation (STD) is applied to SMAP SSS data in the longitude–latitude domain. Data points are rejected when SSS anomalies, computed relative to the first-guess field, exceed thresholds of 7, 6, and 5 STDs in the regions of low variability (STD < 0.1 psu), moderate variability (0.1 < STD < 0.2 psu), and high variability (STD > 0.2 psu), respectively. The spatial distribution of the SSS STD used in this analysis is derived from time series of OISSS v2.0 fields during the period September 2011 - august 2021.

4.4.3. SMOS SSS data

SMOS SSS data are processed in the same way as SMAP SSS data (sec. 4.4.2). An example of data filtering is presented in Figure 10.

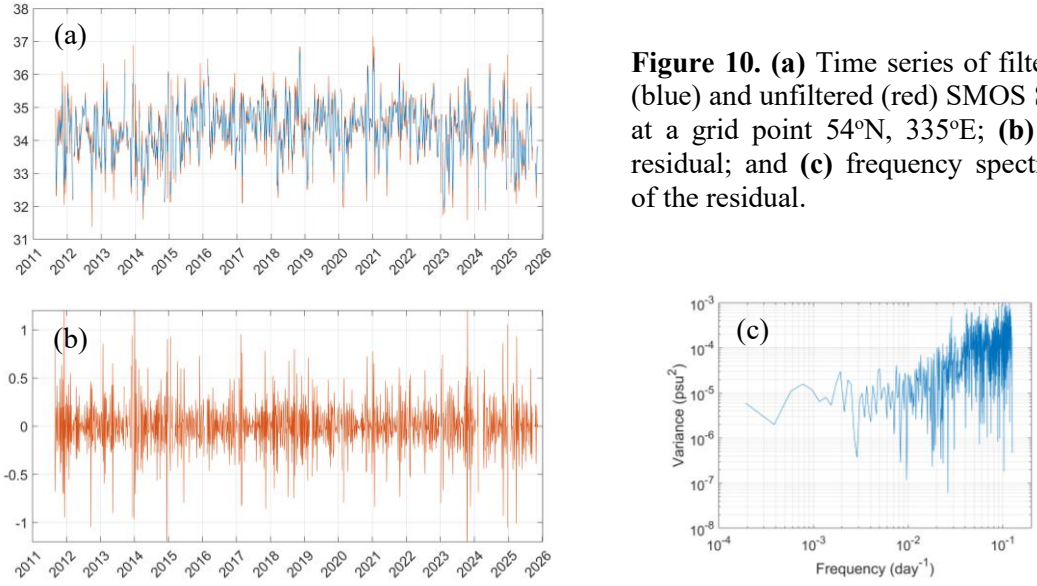

Figure 10. (a) Time series of filtered (blue) and unfiltered (red) SMOS SSS at a grid point 54°N, 335°E; **(b)** the residual; and **(c)** frequency spectrum of the residual.

5. Optimum Interpolation (OI) algorithm

5.1 General description

The interpolation expression for OI with N observations can be written as (Bretherton et al., 1976; Le Traon et al., 1998):

$$\hat{S}_x = S_x^0 + \sum_{i=1}^{N}\sum_{j=1}^{N} A_{ij}^{-1} C_{xj} (S_i^{obs} - S_i^0), \qquad (2)$$

where $\hat{S}_x$ is the interpolated value (or estimate) at the grid point $\mathbf{x}$; S_x^0 is the forecast (or "first guess") value at the grid point $\mathbf{x}$; S_i^{obs} is the measured value at the observation point i: $S_i^{obs} = S_i + \varepsilon_i$, where ε_i is random measurement error; S_i^0 is the forecast value at the observation point i; $\mathbf{A}$ is the $N \times N$ covariance matrix of the data

$$A_{ij} = < (S_i - S_i^0)(S_j - S_j^0) > + < \varepsilon_i \varepsilon_j >; \qquad (3)$$

and $\mathbf{C}$ is the joint covariance of the data and the field to be estimated

$$C_{xj} = < (S_x - S_x^0)(S_j - S_j^0) >. \qquad (4)$$

In (3) and (4), it is assumed that the errors and the field are not correlated.

The OI analysis is formulated relative to a first-guess field, which is assumed to be a good approximation of the true state. The estimate and the observations are then equal to the first guess plus small increments. Accordingly, a grid-point analysis involves interpolating the first-guess field to the observation locations, followed by interpolating the differences between the observations and the first-guess values back to the grid. The final analysis at each grid point is obtained by adding the resulting increment to the first-guess field.

5.2. Specifics

The OI method assumes that the first-guess field and the statistical properties of the field to be analyzed are known prior to the analysis. These parameters are defined as follows.

5.2.1. First guess

The first-guess fields are derived from a compilation of Argo-based products (monthly mean SSS fields). These products are the same as those used to evaluate satellite biases (see Sections 4.3.1 and 4.3.2 for a complete list). An example for the last week of August 2011 is shown in Figure 11. The Argo-derived SSS fields are selected because they are

independent of the analysis of the satellite data and thus provide an unbiased estimate of the first-guess field.

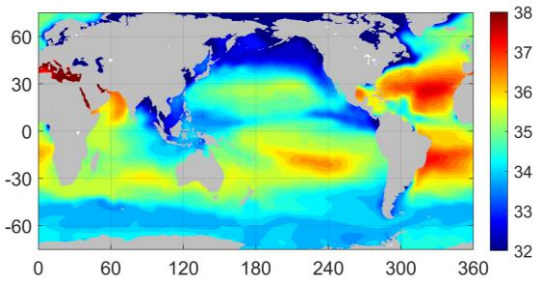

Figure 11. First guess SSS field for the week centered on August 28, 2011.

5.2.2. Signal statistics

The normalized spatial covariance of SSS anomalies is described by the Gaussian function of the form

$$C(r_x, r_y, t) = exp(-r_x^2/R_x^2 - r_y^2/R_y^2), \quad (5)$$

where r_x and r_y are spatial lags in the zonal and meridional directions, respectively, and R_x, R_y are the zonal and meridional correlation scales.

The normalized temporal covariance of SSS anomalies is described by the Gaussian function of the form

$$C(t) = exp(-t^2/T^2), \quad (6)$$

where t is time lag, and T is the correlation time scale.

The Gaussian form of the correlation structures (5) and (6) is chosen because the associated spectrum is positive everywhere and because the resulting covariance matrixes are always positive definite (Weber and Talkner, 1993). The latter is a strict requirement on the choice of a possible analytical form of the correlation function in the OI analysis (Bretherton et al., 1976).

The zonal and meridional correlation scales in Eq. (5) vary as a function of latitude. In OISSS v3.0, the functional form of the spatial correlation scales has been revised to better accommodate higher-resolution input data and to more closely align with the scales observed by SMAP and SMOS, as reported in Yi et al. (2022). Based on the observed scales, the latitudinal dependence of R_y [km] is represented by the following functional form

$$R_y(y) = 26\, exp(-(y-4)^2/225)) + 72, \quad (7)$$

where y is latitude in degrees. The meridional scales are larger in the tropics (98 km at 4°N) than at high latitudes (~72 km).

The zonal correlation scales at mid- and high latitudes are set to equal the meridional scales, while in the tropics they are scaled to represent the zonal elongation of correlation as follows

$$R_x(y) = R_y(y)(0.3\,exp(-(y-4)^2/56.25) + 1). \qquad (8)$$

Near the equator, the aspect ratio R_x / R_y equals 1.3 (R_x = 127 km at 4°N) and gradually decreases with increasing latitude (Figure 12). Poleward of approximately 20°, the correlation function (5) becomes isotropic, with $R_x = R_y$ ≅80 km at 20° latitude. The assumption of zonal anisotropy in the correlation scales is supported by previous observational studies (e.g., Delcroix et al., 2005; Reverdin et al., 2007) as well as by the analysis of satellite-derived SSS data (Yi et al., 2022).

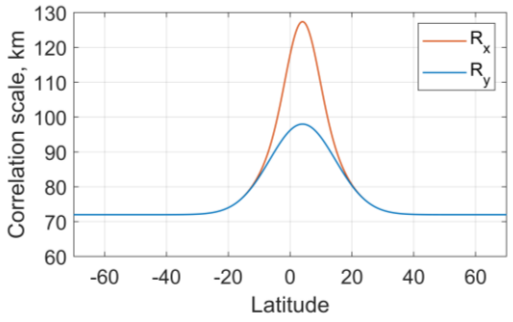

Figure 12. Meridional (blue) and zonal (red) correlation scales applied in the OISSS v3.0 analysis.

The temporal correlation scale is set to T =8 days. This provides a smooth map-to-map transition while preventing the time series from over-smoothing.

5.2.3. Error statistics

5.2.3.1. Aquarius SSS data

Analysis of Aquarius along-track SSS data reveals the presence of long-wavelength errors, hereafter referred to as inter-beam biases, which exhibit spatial correlation over long distances along the satellite tracks. To incorporate statistical information about these errors into the OI scheme, the following error covariance model for the Aquarius data is introduced (Melnichenko et al., 2014):

$< \varepsilon_i \varepsilon_j >= \delta_{ij}\sigma_w^2 + \sigma_L^2$ -if data points i, j are on the same track and beam, and in the same cycle, and

$< \varepsilon_i \varepsilon_j >= \delta_{ij}\sigma_w^2$ -otherwise,

where δ_{ij} is the Kronecker delta, σ_w^2 is the variance of the uncorrelated (white) noise, and σ_L^2 is the variance of the long-wavelength (along-track) error.

Given prior filtering of Aquarius Level 2 SSS data (section 4.4.1), the variance of the white noise is assumed to be 10% of the signal variance, independent of the geographical location. The long-wavelength error correlation structure is represented by the exponential function of the form

$$C_L(l) = exp(-l/R_L) \qquad (9)$$

where l is the along track separation distance and $R_L = 500$ km is the exponential decay scale. The estimate of R_L is obtained by fitting the curve (9) to the inter-bean bias statistics evaluated by comparison of the covariances of the inter-beam differences for Aquarius and ancillary SSS data as described in Melnichenko et al. (2014) and shown in Figure 13.

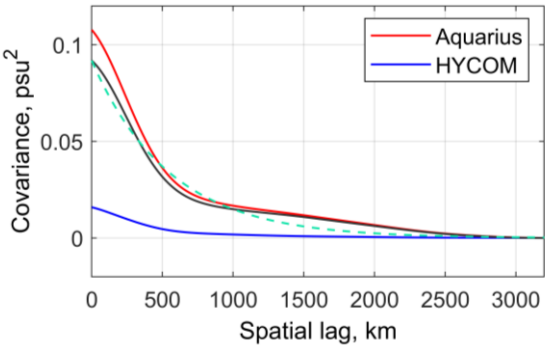

Figure 13. Autocovariances of inter-beam differences computed from the data of the North Atlantic (0°–40°N). Red and blue curves represent Aquarius and ancillary SSS, respectively. The black curve is the difference between the two, representing the covariance of the long-wavelength error in Aquarius data. Its approximation by the exponential function is shown by the green dashed curve. From Melnichenko et al. (2014).

The variance of the long-wavelength error varies with latitude from about 0.04 psu^2 in the tropics to 0.1 psu^2 at high latitudes. Following the latitudinal changes in both the error and signal variances (not shown in figure), the ratio of the error variance to the signal variance, η, is approximated by the following analytical curve

$$\eta = 2 * (1 - exp(-y^2/400))/1.43) + 0.3. \qquad (10)$$

Thus, the relative variance of the long-wavelength error is set to vary from 30% in the equatorial region, where the signal variance is large, to more than 150% at high-latitudes, where the error variance is large.

5.2.3.2. SMAP SSS data

The error covariance matrix consists of one part, $< \varepsilon_i \varepsilon_j >= \sigma_w^2$, and represents uncorrelated errors. The variance of the uncorrelated error is assumed to be 50% of the signal variance, independent of the geographical location.

5.2.3.3. SMOS SSS data

Random errors in SMOS SSS data are assumed to be uncorrelated. The variance of the uncorrelated error is assumed to be 50% of the signal variance, independent of the geographical location.

5.3. Implementation

The OISSS v3.0 analysis is performed in two steps.

Step1. Spatial OI is applied to map SSS data onto a 0.25° × 0.25° longitude–latitude grid at 4-day intervals, beginning in September 2011. For this stage of the analysis, the input data are grouped into 4-day time steps, as illustrated schematically in Figure 14. At each 4-day step, data are selected using satellite-specific temporal search windows: 7 days for Aquarius, 4 days for SMAP, and 9 days for SMOS. These intervals are chosen to account for the differing revisit times of each satellite as well as the level of noise in the corresponding SSS data. SMAP and SMOS observations are binned onto the 0.25° × 0.25° spatial bins and then averaged together to reduce noise. This approach assumes that the random errors in SMAP and SMOS measurements are uncorrelated.

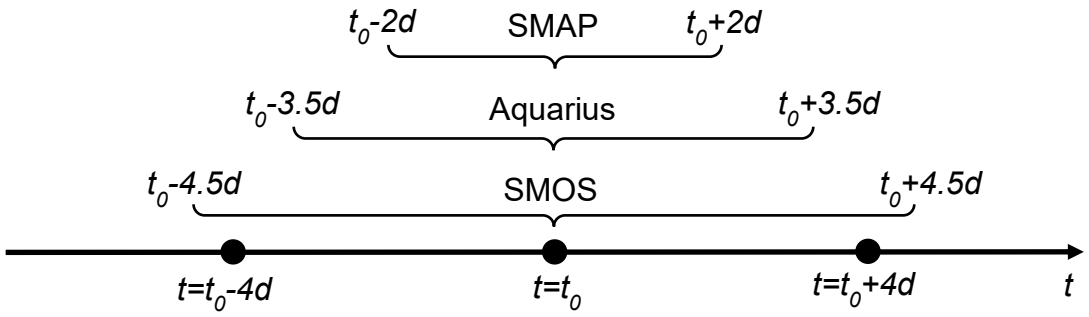

Figure 14. Aquarius, SMAP and SMOS data pre-processing for spatial OI. At each 4-day time step, observations are grouped into n-day data blocks and time averaged within each block.

The OI analysis is performed using a local approximation; that is, only data points within a limited subdomain surrounding each analysis grid point are considered. The radius of this subdomain is defined as four times the spatial correlation scale, which allows for accommodating both the signal and error correlation (for the case of Aquarius data; section 4.3.1). This local approximation also mitigates the effects of spatial inhomogeneity in the signal and error statistics (Weber and Talkner, 1993).

Step 2. Temporal OI is applied to the 4-day SSS maps (at each grid point) to generate daily time series. The temporal correlation scale (Eq. 6) is set to 8 days, providing a smooth transition between successive maps while avoiding over-smoothing.

5.4. Uncertainty estimate

5.4.1. Empirical uncertainty

The uncertainty is estimated empirically by comparing daily OISSS maps with concurrent Argo buoy data. Argo buoy salinity measurements in the near-surface layer (depth <10 m) are assumed to represent in-situ SSS. The error statistics are computed by comparing buoy measurements for a given day $\pm$3.5 days with SSS values at the same locations obtained by interpolating the corresponding OISSS maps. Uncertainties are estimated in 8^{o}-longitude x 8^{o}-latitude bins as the RMSDs between the OISSS maps and the corresponding buoy data. The coarse resolution RMSD map is then interpolated onto the analysis grid to provide estimates of the uncertainty. In the areas lacking buoy observations, the uncertainties are estimated by extrapolating from adjacent regions. The estimated empirical uncertainty includes the so-called sampling error which arises due to unresolved small-scale SSS variability (see Sec. 6.2).

5.4.2. Formal uncertainty

The formal uncertainty for each OISSS field is estimated by propagating the uncertainties of the Level 2 SSS retrievals (as provided by the data producers) using standard error propagation techniques (Taylor, 1982). An example is shown in Figure 15. To create monthly fields, the decorrelation time scale is assumed to be T=8 days; thus, there are 4 independent observations in the monthly mean, and the error reduction is by a factor of 2.

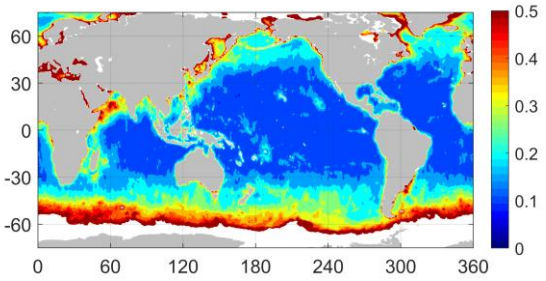

Figure 15. Formal uncertainty for the daily OISSS field centered on July 9, 2016. The uncertainties are typically large along the coastline and in polar latitudes (cold water).

5. Global OISSS fields

Daily (8-day time scale) SSS

Time series of daily (8-day time scale) SSS fields are produced by the OISSS algorithm.

Monthly SSS

For each calendar month, the mean SSS field is computed as the average of the daily OI SSS fields within that month.

Monthly climatological mean SSS

Monthly climatological mean SSS fields are computed by averaging the corresponding monthly SSS fields over the 10-year period from September 2011 to August 2021.

Monthly SSS anomaly

Monthly SSS anomalies are computed by subtracting the corresponding monthly climatological means. This procedure removes the mean seasonal cycle and returns month-to-month inter-annual variations.

5.1. Spatial coverage and resolution

Figure 16 presents example plots of OISSS fields. The central panel (Figure 16a) provides a global view, illustrating the spatial coverage of the product. The OISSS v3.0 dataset covers the global ocean, including the Arctic and Antarctic in ice-free regions. The dataset also captures coastal regions and marginal seas, such as the South China Sea and the Gulf of Mexico, as well as semi-enclosed seas, including the Mediterranean and the Baltic Sea, where high-quality Level 2 data are available.

The resolution capabilities of the OISSS analysis can be inferred from the regional maps presented in Figure 16. Figure 16c, for example, provides a zoomed view of a broad area in the North Atlantic. Among the features depicted is a frontal structure associated with the Gulf Stream and its extension, separating low-salinity slope waters from the more saline waters of the Sargasso Sea. Another prominent feature is the shelf-break front, which delineates fresher shelf waters from saltier slope waters and extends from Cape Hatteras—where the Gulf Stream separates from the coast—to Nova Scotia. Between these features, several mesoscale circular structures, commonly referred to as Gulf Stream rings, are observed. Their temporal evolution is illustrated in a sequence of maps shown on the right side of the figure.

Another prominent example is observed in the eastern tropical Pacific. Figure 16d illustrates the SSS signature of Tropical Instability Waves (TIWs), which appear as cusp-like features between approximately 0° and 5°N, with a wavelength of about 1,000 km (~10° of longitude). These waves exhibit a dominant period of approximately 30 days and propagate westward at a speed of about 0.5 m s^{-1} (not shown in the figure).

These examples demonstrate that the spatial resolution of the OISSS analysis is sufficient to resolve large mesoscale features and frontal structures. The effective spatial resolution of the product is estimated to be on the order of 60 km (length scale).

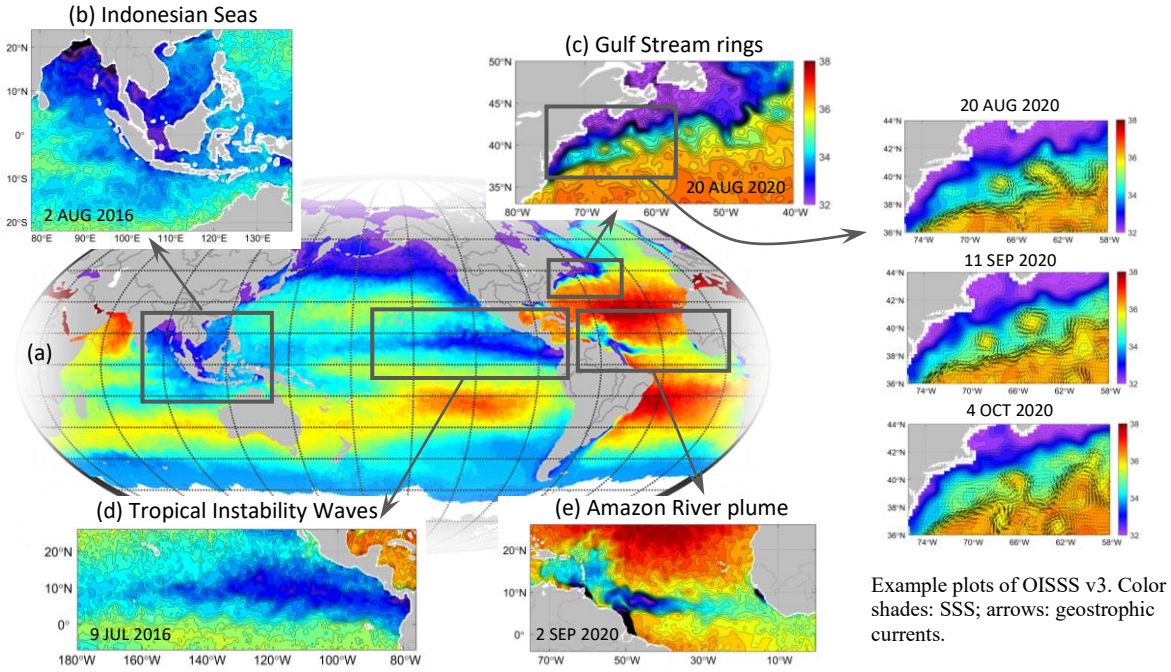

Example plots of OISSS v3. Color shades: SSS; arrows: geostrophic currents.

Figure 16. Example plots of OISSS v3.0.

5.2. Validation

OISSS Version 3.0 is validated using the same methodology used for previous versions of the analysis.

Near-surface salinity observations from Argo buoys are used to estimate the error statistics of the OISSS analysis. The Argo network provides a quasi-random geographical distribution of approximately 1,100 in situ salinity measurements per week. Only measurements shallower than 10 m and flagged as high quality from each Argo profile are included in this analysis. Error statistics are computed by comparing buoy measurements for a given week (7-day search window) with SSS values at the same locations, obtained by interpolating the corresponding OISSS fields. The validation results include all areas where the in-situ data are available, including coastal areas, cold water, and internal seas.

Figure 17 shows the time series of the bias (defined as the mean difference between the product and buoy observations across all buoy locations) and the root-mean-square difference (RMSD) for the OISSS v3.0 analysis, evaluated against concurrent Argo buoy observations. The product exhibits a global bias that fluctuates around zero (Figure 17a), with a standard deviation of 0.028 psu. The RMSD between the OISSS analysis and the concurrent buoy data fluctuates around 0.2 psu (Figure 17b), with a mean value of 0.22 psu over the period September 2011–August 2025.

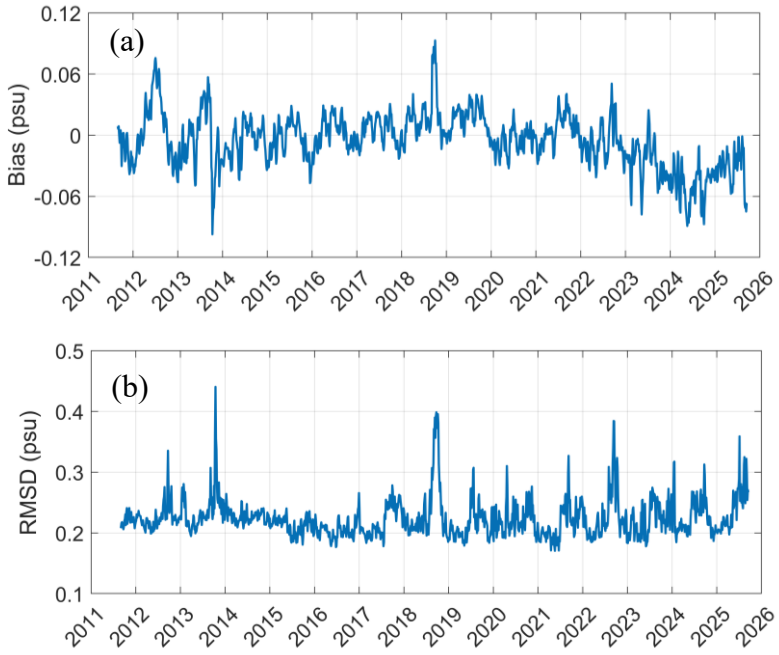

Figure 17. (a) Weekly mean differences and (b) RMSD between the OISSS v3.0 maps and Argo buoy data.

The geographical distribution of the mean bias and RMSD for the OISSS v3.0 analysis is shown in Figure 18. The mean bias and RMSD were computed in 8-degree spatial bins from the differences between the weekly OISSS maps (every fourth day from the daily time series) and the corresponding in-situ observations. The bin size was selected to ensure an adequate number of collocations (>100) in each bin.

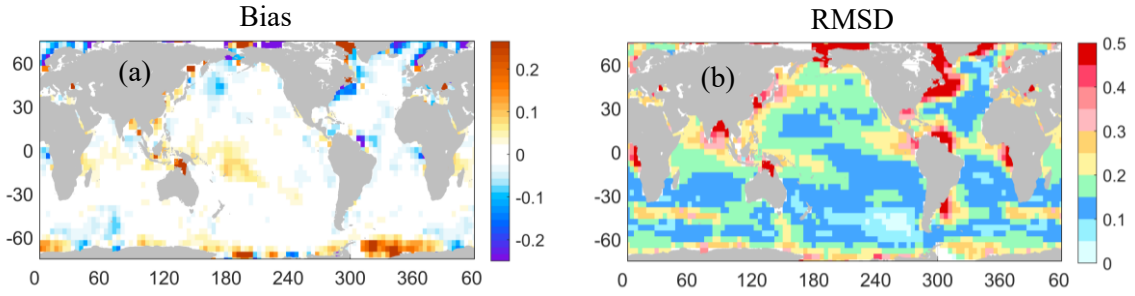

Figure 18. Geographical distribution of the (a) mean bias and (b) RMSD between the weekly OISSS v3.0 maps and in-situ buoy data over the period September 2011 through August 2025.

The mean bias is close to zero across most of the open ocean, except for a few regions in the Southern Ocean and the Arctic (figure 18a). Persistent negative biases (i.e., satellite-derived sea surface salinity is fresher than buoy measurements) are evident near the outflows of major rivers, such as the Amazon in the North Atlantic, and along the east coast of the United States. Some of these negative differences can be attributed to strong vertical salinity gradients in the near-surface layer, such that salinity at approximately 5 m depth, sampled by typical Argo floats, differs substantially from the surface salinity measured by

satellites. Other differences, particularly positive differences, are likely associated with incomplete bias correction.

The largest RMSDs (Figure 18b), exceeding 0.2 psu, are observed in regions of pronounced SSS variability, including the Intertropical Convergence Zones in the North Pacific and North Atlantic, the South Pacific Convergence Zone, the Gulf Stream, and areas influenced by major river outflows such as the Amazon in the North Atlantic (see Figure 19). However, these relatively large discrepancies between OISSS maps and buoy observations do not necessarily indicate errors in the satellite measurements or the mapping procedure. Rather, they may arise from (i) strong vertical salinity gradients in the near-surface layer and/or (ii) unresolved spatial and temporal variability. In regions with sharp SSS gradients, differences between point measurements from buoys and area-averaged satellite estimates (or gridded OISSS) can exceed 0.2 psu (Vinogradova and Ponte, 2012, 2013).

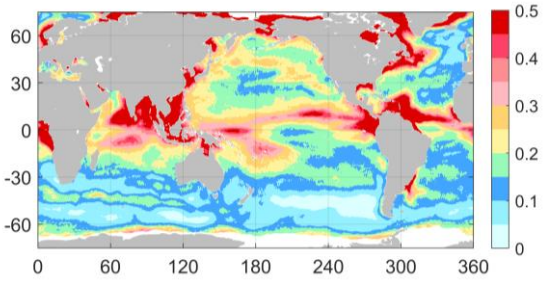

Figure 19. The standard deviation of SSS computed from daily time series of OISSS fields for the period September 2011 through August 2025.

The histogram distribution of the differences between the OISSS analysis and buoy data is presented in Figure 20a. Overall, the OISSS estimates have a good agreement with the buoy data and the histogram distribution of the differences is quite narrow. Approximately 51% of the differences are less than 0.1 psu and more than 78% are less than 0.2 psu. The proportion of outliers, defined as the differences larger than 0.5 psu (1 psu) is less than 3% (1%). The geographical distribution of these outliers is shown in Figure 20b. Most outliers are in the regions characterized by strong SSS variability (see Figure 19), consistent with the spatial pattern of sampling error (Vinogradova and Ponte, 2013; their Figure 2).

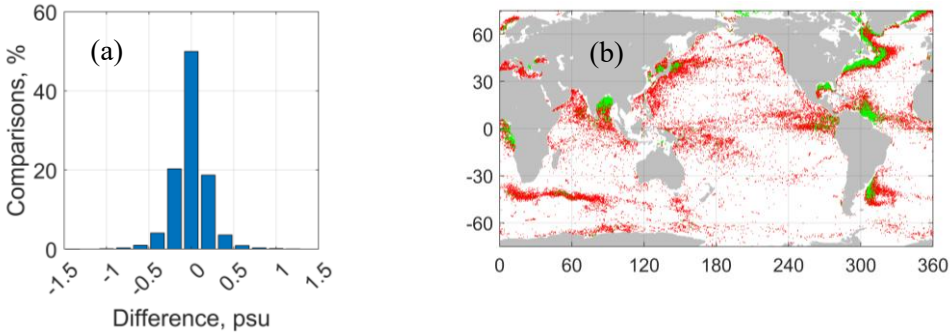

Figure 20. (a) Statistics of the differences between Argo buoy data and the OISSS analysis. (b) Locations of 'outliers', defined as the differences large than 0.5 psu (red dots) and 1 psu (green dots). The error statistics are computed by comparing Argo buoy measurements for a given week with SSS values at the same locations obtained by interpolation of the corresponding OISSS maps.

The zonally averaged differences between the weekly OISSS maps and the corresponding buoy observations are shown in Figure 21. Residual biases, exhibiting a clear seasonal cycle, are apparent at high latitudes during 2011–2015 and in the northern tropics during 2024–2025. The latter biases are likely related undetected RFI contamination in parts of the Bay of Bengal, the South China Sea, and along the east coast of Japan.

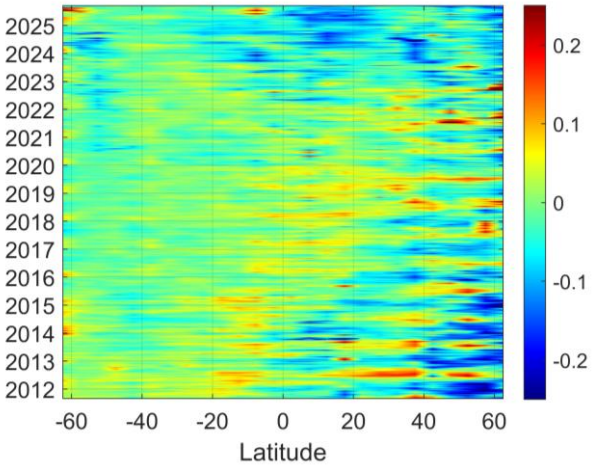

Figure 21. Latitude-time distribution of the zonally averaged differences (psu) between the weekly OISSS maps and the corresponding Argo buoy data. The error statistics were computed by comparing Argo buoy observations for a given week with SSS values at the same locations obtained by interpolation of the corresponding OISSS maps. The zonally averaged biases were computed by averaging these statistics over 5-degree latitude bands.

Beginning in late 2023, SSS estimates derived from measurements made by the SMAP and SMOS satellites have been increasingly affected by contamination from RFI, attributed primarily to military activities in regions experiencing geopolitical conflicts. The affected areas include the Bay of Bengal, Gulf of Thailand, Mediterranean Sea, northern Europe, Black Sea, Caspian Sea, Arabian Sea, and the South China Sea (Meissner and Manaster, 2025). The OISSS processing algorithm excludes observations flagged as RFI-contaminated, which can lead to substantial data gaps in these regions. An example is shown in Figure 22.

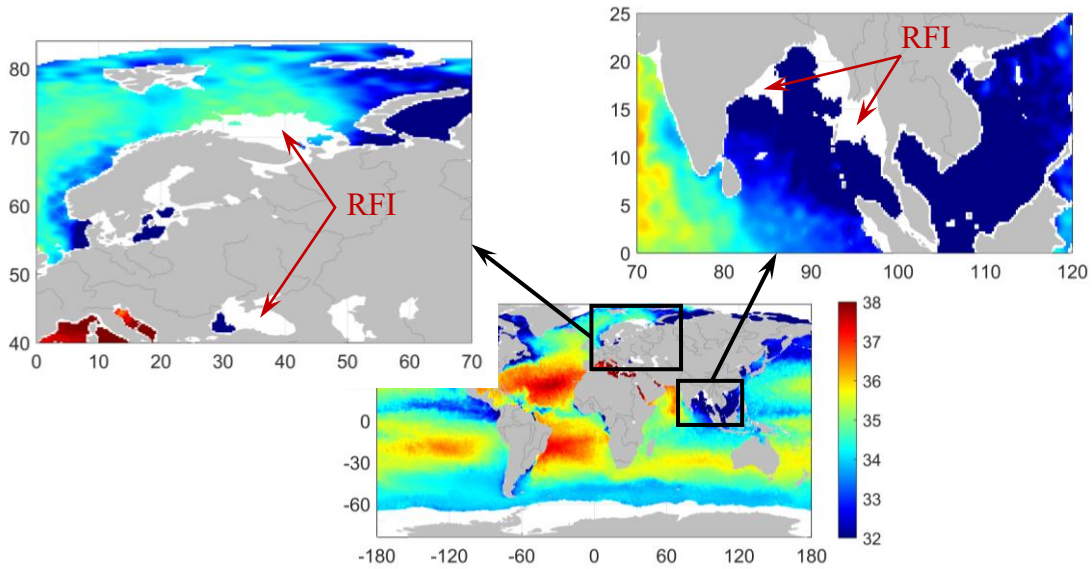

Figure 22. OISSS v3.0 for October 15, 2024

Observations affected by RFI (undetected RFI) may still be present in adjacent areas (undetected RFI; not flagged) and users are advised to exercise caution when interpreting SSS variability in these areas.

Despite significant effort taken to reduce errors and biases in the satellite SSS data, the resulting OISSS maps may still have errors and biases, both globally and regionally. **We encourage users to continue to validate the OISSS dataset and quantify noise and errors in their research. We are especially interested in receiving feedback on the utility of the product and potential issues relevant to noise and biases, especially from regional studies, which may have access to higher quality and enhanced resolution in-situ data sets.**

Comments, questions regarding the OISSS dataset and requests for the data can be directed to

Dr. Oleg Melnichenko
Earth and Space Research
Email: oleg@esr.org

8. Acknowledgements

This project was supported by the National Aeronautics and Space Administration (NASA) Ocean Salinity Science Team through grant 80NSSC22K0265. The Argo data were collected and made freely available by the International Argo Program and the national programs that contribute to it (https://www.ocean-ops.org). The Argo Program is part of the Global Ocean Observing System. The authors acknowledge the many constructive dialogues with the members of the NASA Ocean Salinity Science Team.

10. References

AQUARIUS USER GUIDE, Dataset Version 5.0. Guide Version: 8.0, November 27, 2017. JPL D-70012 AQ-010-UG-0008. JPL URS CL#: 17-5944. Document accessed 2018-05-03 at http://dx.doi.org/10.5067/DOCUM-AQR01.

Bretherton, F. P., R.E Davis, and C.B. Fandry, 1976: A technique for objective analysis and design of oceanographic experiments applied to MODE-73, *Deep Sea Res.*, **23**, 559-582.

Boutin, J., J.L. Vergely, S. Marchand, F. D'Amico, A. Hasson, N. Kolodziejczyk, N. Reul, G. Reverdin, and J. Vialard (2018), New SMOS Sea Surface Salinity with reduced systematic errors and improved variability, *Remote Sens. Environ.*, 214, 115-134.

Delcroix, T., M.J. McPhaden, A. Dessier, and Y. Gouriou, 2005: Time and space scales for sea surface salinity in the tropical ocean, *Deep-Sea Res. I*, **52**, 787-813.

Good, S.A., M.J. Martin, and N.A. Rayner (2013). EN4: quality controlled ocean temperature and salinity profiles and monthly objective analyses with uncertainty estimates, *J. Geophys. Res. Oceans*, 118, 6704-6716, doi:10.1002/2013JC009067.

Hosoda, S., T. Ohira, and T. Nakamura, 2008: A monthly mean dataset of global oceanic temperature and salinity derived from Argo float observations, *JAMSTEC Rep. Res. Dev.*, Vol. 8, 47-59.

Kao, H.-Y., G.S.E. Lagerloef, T. Lee, O. Melnichenko., T. Meissner, and P. Hacker, 2018: Assessment of Aquarius Sea Surface Salinity, *Remote Sensing*, 10(9), 1341, doi:10.3390/rs/10091341.

Kolodziejczyk, N., A. Prigent-Mazella, and F. Gaillard, 2021: ISAS temperature and salinity gridded fields. SEANOE. https://doi.org/10.17882/52367

Lagerloef, G., F.R. Colomb, D. LeVine, F. Wentz, S. Yueh, C. Ruf, J. Lilly, J. Gunn, Y. Chao, A. deCharon, G. Feldman, and C. Swift, 2008: The Aquarius/SAC-D Mission: Designed to meet the salinity remote-sensing challenge, *Oceanography*, **20**, 68-81.

Le Traon, P.Y., F. Nadal, and N. Ducet, 1998: An improved mapping method of multisatellite altimeter data, *J. Atmos. Oceanic Technol.*, **15**, 522-534.

Le Vine, D.M., G.S.E. Lagerloef, F.R. Colomb, S.H. Yueh, and F.A. Pellerano, 2007: Aquarius: An instrument to monitor sea surface salinity from Space, *IEEE Transactions on Geoscience and Remote Sensing*, **45**, 2040-2050.

Meissner, T., F.J. Wentz, and D.M. Le Vine, 2017: Aquarius Salinity Retrieval Algorithm End of Mission ATBD, report number 120117, Remote Sensing Systems, Santa Rosa, CA, 113 pp. Available online at http://images.remss.com/papers/tech_reports/2017/Meissner_AQ_ATBD_EOM_final.pdf

Meissner, T., F.J. Wentz, and D.M. Le Vine, 2018: The Salinity Retrieval Algorithms for the NASA Aquarius Version 5 and SMAP Version 3 Releases, Remote Sensing 10, 1121, doi:10.3390/rs10071121.

Meissner, T., F. J. Wentz, A. Manaster, R. Lindsley, M. Brewer, M. Densberger, 2024: Remote Sensing Systems SMAP Ocean Surface Salinities [Level 2C, Level 3 Running 8-day, Level 3 Monthly], Version 6.0 validated release. Remote Sensing Systems, Santa Rosa, CA, USA. Available online at www.remss.com/missions/smap**.**

Meissner, T., and A. Manaster, 2025: Detection and Flagging of Radio Frequency Interference Contamination in SMAP Ocean Observations. *J. Atmos. Oceanic Technol.*, 42, 1585–1600, https://doi.org/10.1175/JTECH-D-25-0062.1.

Melnichenko, O., P. Hacker, N. Maximenko, G. Lagerloef, and J. Potemra, 2014: Spatial Optimal Interpolation of Aquarius Sea Surface Salinity: Algorithms and Implementation in the North Atlantic, *J. Atmos. Oceanic Technol.*, 31, 1583-1600.

Melnichenko, O., P. Hacker, N. Maximenko, G. Lagerloef, and J. Potemra, 2016: Optimum interpolation analysis of Aquarius sea surface salinity, *J. Geophys. Res. Oceans,* 121, 602-616, doi:10.1002/2015JC011343.

Reul, N.; Grodsky, S.A.; Arias, M.; Boutin, J.; Catany, R.; et al, 2020: Sea surface salinity estimates from spaceborne L-band radiometers: An overview of the first decade of observation (2010–2019), *Remote Sens. Environ.*, 242, 111769, doi:10.1016/j.rse.2020.111769.

Reul, N., M. Arias, P. Spurgeon, et a., 2017: Read-me-first note for SMOS Level 2 Sea Surface Salinity data products, ESA, 10 May 2017, available online at https://earth.esa.int/documents/10174/1854503/SMOS-Level-2-Ocean-Salinity-v662-release-note.

Reverdin, G., E. Kestenare, C. Frankignoul, and T. Delcroix, 2007: Surface salinity in the Atlantic Ocean (30ºS-50ºN), *Prog. Oceanogr.*, **73**, 311-340.

Roemmich, D. and J. Gilson, 2009: The 2004-2008 mean and annual cycle of temperature, salinity, and steric height in the global ocean from the Argo Program. *Prog. Oceanogr*., 82, 81-100.

Taylor, J.R., 1982: *An introduction to Error Analysis: The Study of Uncertainties in Physical Measurements*, Univ. Sci. Books, Mill Valley, CA

Vinogradova, N. T., and R.M. Ponte, 2012: Assessing temporal aliasing in satellite-based surface salinity measurements, *J. Atmos. Oceanic Technol.*, 29, 1391-1400, doi:10.1175/JTECH-D-11-00055.1.

Vinogradova, N. T., and R.M. Ponte, 2013: Small-scale variability in sea surface salinity and implications for satellite-derived measurements, *J. Atmos. Oceanic Technol.*, **30**, 2689-2694.

Weber, R.O., and P. Talkner, 1993: Some Remarks on Spatial Correlation Function Models, *Mon. Wea. Rev.*, **121**, 2611-2617.

Yi, Daling Li, Oleg Melnichenko, Peter Hacker, and Ke Fan. 2022. "Satellite-Observed Time and Length Scales of Global Sea Surface Salinity Variability: A Comparison of Three Satellite Missions" *Remote Sensing* 14, no. 21: 5435. https://doi.org/10.3390/rs14215435.

9. Data format specification

9.2.1. Daily (8-day time scale)

File name: OISSS_L4_multimission_global_daily_v3.0_yyyy-mm-dd.nc
yyyy = 4-digit year, mm= 2-digit month of year, dd= 2-digit day of month

Grid and dimensions: monthly OISSS fields are provided on a regular 0.25°-longitude x 0.25°-latitude Earth grid. Xdim=1440; Ydim=720. Time (T) corresponds to the day on the calendar.

Variables:

'**sss**' (T, Xdim, Ydim) – sea surface salinity (SSS);

'**sss_empirical_uncertainty**' (T, Xdim, Ydim) – estimated empirical uncertainty of the multi-mission OISSS;

'**sss_formal_uncertainty**' (T, Xdim, Ydim) – estimated formal uncertainty of the multi-mission OISSS;

9.2.2. Monthly

For each month, the monthly mean, monthly climatological mean and monthly anomaly data are provided in the same file.

File name: OISSS_L4_multimission_global_monthly_v3.0_yyyy-mm.nc
yyyy = 4-digit year, mm= 2-digit month of year

Grid and dimensions: monthly OISSS fields are provided on a regular 0.25°-longitude x 0.25°-latitude Earth grid. Xdim=1440; Ydim=720. Time (T) corresponds to the middle date of the month.

Variables:

'**sss**' (T, Xdim, Ydim) – monthly mean SSS;

'**sss_empirical_uncertainty**' (T, Xdim, Ydim) – estimated empirical uncertainty of the multi-mission OISSS monthly average;

'**sss_formal_uncertainty**' (T, Xdim, Ydim) – estimated formal uncertainty of the multi-mission OISSS monthly average;

‘**sss_climatology**’ (T, Xdim, Ydim) – monthly climatological SSS based on the multi-mission OISSS dataset from September 2011 to August 2021.

‘**sss_anomaly**’ (T, Xdim, Ydim) – SSS anomaly relative to the product-based monthly climatology.